



**HAL**  
open science

## Evaluation of electrochemical performances of ZnFe<sub>2</sub>O<sub>4</sub>/[gamma]-Fe<sub>2</sub>O<sub>3</sub> nanoparticles prepared by laser pyrolysis

Samantha Bourrioux, Luyuan Paul Wang, Youri Rousseau, Pardis Simon, Aurélie Habert, Yann Leconte, Moulay Tahar Sougrati, Lorenzo Stievano, Laure Monconduit, Zhichuan J. Xu, et al.

### ► To cite this version:

Samantha Bourrioux, Luyuan Paul Wang, Youri Rousseau, Pardis Simon, Aurélie Habert, et al.. Evaluation of electrochemical performances of ZnFe<sub>2</sub>O<sub>4</sub>/[gamma]-Fe<sub>2</sub>O<sub>3</sub> nanoparticles prepared by laser pyrolysis. *New Journal of Chemistry*, 2017, 41 (17), pp.9236-9243. 10.1039/C7NJ00735C . cea-01567338

**HAL Id: cea-01567338**

**<https://cea.hal.science/cea-01567338>**

Submitted on 22 Jul 2017

**HAL** is a multi-disciplinary open access archive for the deposit and dissemination of scientific research documents, whether they are published or not. The documents may come from teaching and research institutions in France or abroad, or from public or private research centers.

L'archive ouverte pluridisciplinaire **HAL**, est destinée au dépôt et à la diffusion de documents scientifiques de niveau recherche, publiés ou non, émanant des établissements d'enseignement et de recherche français ou étrangers, des laboratoires publics ou privés.



Distributed under a Creative Commons Attribution 4.0 International License

## Evaluation of electrochemical performances of ZnFe<sub>2</sub>O<sub>4</sub>/γ-Fe<sub>2</sub>O<sub>3</sub> nanoparticles prepared by laser pyrolysis

Samantha Bourrioux<sup>1</sup>, Luyuan Paul Wang<sup>2</sup>, Youri Rousseau<sup>1</sup>, Pardis Simon<sup>3</sup>, Aurélie Habert<sup>1</sup>, Yann Leconte<sup>1</sup>, Moulay Tahar Sougrati<sup>4</sup>, Lorenzo Stievano<sup>4</sup>, Laure Monconduit<sup>4</sup>, Zhichuan J. Xu<sup>2</sup>, Madhavi Srinivasan<sup>2</sup>, Alain Pasturel<sup>5</sup>

<sup>1</sup>CEA, IRAMIS, NIMBE, CNRS UMR 3685, F- 91191, Gif-sur-Yvette, France

<sup>2</sup>School of Materials Science and Engineering, Nanyang Technological University, Singapore

<sup>3</sup>Laboratoire Interdisciplinaire Carnot de Bourgogne, UMR 6303 CNRS-Univ. Bourgogne Franche-Comté, 9, avenue Alain Savary, 21078 Dijon, France

<sup>4</sup>Institut Charles Gerhardt-CNRS Université Montpellier II Place Eugène Bataillon, 34095 Montpellier, France

<sup>5</sup>SIMAP, UMR CNRS 5266, Grenoble INP, BP 75, 38402 Saint-Martin d'Hères Cedex, France

### Abstract

A ZnFe<sub>2</sub>O<sub>4</sub>/γ-Fe<sub>2</sub>O<sub>3</sub> nanocomposite (theoretical specific capacity: 1002 mAh/g) was successfully synthesized by laser pyrolysis, a very attractive nanosynthesis technique characterized by high versatility and flexibility. The obtained nanopowder was thoroughly characterized by XRD, XPS, Mössbauer spectroscopy and HRTEM, which confirmed the presence of the two phases. A bimodal size distribution with small particles (tens of nanometers) and large ones (above 500 nm) was revealed by SEM and TEM. The ZnFe<sub>2</sub>O<sub>4</sub>/Fe<sub>2</sub>O<sub>3</sub> nanocomposite was tested as negative electrode material for lithium-ion batteries, showing significantly improved lithium storage properties with a high reversible capacity and rate capability compared to pure ZnFe<sub>2</sub>O<sub>4</sub> electrode. A capacity exceeding 1200 mAh/g is sustained after 100 cycles at 100 mA/g, with a gradual increase of the capacity during cycling. At 500 mA/g current rate, a reversible and stable capacity of 360 mAh/g is observed after 300 cycles. Electrochemical measurements with several electrolytes and electrode formulations were also conducted in order to explore the origin of the extra capacity and its increase with cycling.

**Keywords:** laser pyrolysis, synthesis, morphology, composite, high capacity, rate capability, capacity

### Introduction

Lithium-ion batteries have been widely used in portable electronic devices for years. With the depletion of fossil fuels and the growing environmental concerns, lithium-ion batteries also received considerable attention to contribute to the development of electric vehicles and the storage of renewable energies. Most commercial lithium-ion batteries use graphite as anode material, which has a good cycling stability but suffers from a low theoretical capacity (372 mAh/g), limiting the energy density for nomad applications.

New high performance negative electrode materials are thus needed for next generation lithium-ion batteries to address the increasing demand of energy. Due to their high theoretical capacities, conversion materials have been

investigated as potential substitutes to graphite. In particular, a great attention has been devoted to 3d transition metal oxides ( $A_xO_y$  with  $A=Fe, Co, Ni, Mn \dots$ )<sup>1</sup>.

Transition metal oxides such as cobalt or iron oxides have been studied because of their high theoretical capacities, which can be as high as 1000 mAh/g. Good performance was obtained with nanostructured oxides: for example,  $\alpha\text{-Fe}_2\text{O}_3$  nanoflakes exhibit a stable capacity of 680 mAh/g for 80 cycles at  $C/10$  (100 mA/g) current rate<sup>2</sup>, porous  $\text{Co}_3\text{O}_4$  nanotubes show a reversible capacity of 677 mAh/g for 60 cycles at 1C rate<sup>3</sup> and porous hollow  $\text{Fe}_3\text{O}_4$  beads are able to maintain a reversible capacity of 500 mAh/g for 100 cycles at  $C/10$ <sup>4</sup>. However, these materials are not the ideal choice to replace graphite due to their high working voltage vs.  $\text{Li}^+/\text{Li}$  (between 2.1 and 1.9 V vs.  $\text{Li}^+/\text{Li}$  for cobalt and iron oxides) and the toxicity and cost of cobalt. On the contrary, mixed-transition metal oxides with an  $\text{AB}_2\text{O}_4$  spinel crystal structure ( $A, B=Fe, Zn, Mn \dots$ ) provide not only similar theoretical capacities but also the feasibility to tune the working voltage, depending on the chosen transition metals. For instance,  $\text{ZnFe}_2\text{O}_4$  has a working voltage of 1.5 V vs.  $\text{Li}^+/\text{Li}$  which is lower than  $\text{Fe}_2\text{O}_3$  and  $\text{Fe}_3\text{O}_4$  working voltages<sup>5</sup>; also the addition of zinc vs lithium allows the formation of ZnLi alloy during the storage mechanism, leading to an increase of capacity. Moreover, as an abundant, cheap, non-toxic and environmental-friendly material with a high theoretical capacity (1000 mAh/g), zinc ferrite is an interesting substitute for graphite as negative electrode material in lithium-ion batteries.

Several works have reported very promising results for zinc ferrite negative electrodes made with a variety of synthesis processes and with different particles morphologies.  $\text{ZnFe}_2\text{O}_4$  hollow spheres obtained by hydrothermal synthesis are able to cycle for 50 cycles keeping a reversible capacity of 900 mAh/g<sup>6</sup>. Electrospinning technique allows the synthesis of zinc ferrite nanofibers which are able to reach a capacity higher than 700 mAh/g after 30 cycles<sup>7</sup>. To enhance  $\text{ZnFe}_2\text{O}_4$  performance, some studies also focused their efforts on carbon addition to improve the material conductivity and maintain the structure of the material. This can lead to very high capacity materials:  $\text{ZnFe}_2\text{O}_4$  nanoparticles with graphene nanosheets with a reversible capacity around 950 mAh/g after 50 cycles at  $C/10$  current rate<sup>8</sup> or  $\text{ZnFe}_2\text{O}_4$  microspheres with a carbon coating showing a capacity of 1187 mAh/g after hundred cycles at  $C/20$ <sup>9</sup>. The latter showed a capacity higher than the theoretical one and increasing during the first cycles. Several explanations are proposed for these two phenomena: (i) a morphological re-configuration of the electrode during the charge/discharge process that activates additional oxides particles which were not initially reachable by the lithium,<sup>9,10</sup> (ii) a contribution of carbon to the capacity<sup>9,11</sup> or (iii) a reversible reaction of a polymeric layer on the nanoparticles<sup>11</sup>.

Various synthetic processes are available for the synthesis of zinc iron oxides nanopowders with different morphologies including hydrothermal synthesis,<sup>6,12</sup> co-precipitation,<sup>10</sup> urea combustion process<sup>13</sup> and electrospinning<sup>7</sup>. In this paper,  $\text{CO}_2$  laser pyrolysis was used for the first time to synthesize zinc iron oxide nanoparticles. This process is an advantageous one-step versatile and flexible nanosynthesis technique<sup>14</sup>. The control of different operational parameters such as laser power, choice of gases and tuning of their flow rates, as well as the nature and concentration of the precursors, allows the production of nanopowders with various morphologies and crystallinities. It is also a very interesting technique as the precursors can be solid, liquid or gaseous, giving a large range of different possibilities for the tailored synthesis of any compound. It is a scalable route to produce high purity nanomaterials, with a good reproducibility which can be adapted for industrial production. One of the major drawbacks of laser pyrolysis, however, is the need to find a precursor with an absorption band at 10.6  $\mu\text{m}$ , or the use of a sensitizer (mainly  $\text{C}_2\text{H}_4$  or  $\text{NH}_3$ ) sometimes leading to carbon or nitrogen pollution.

Herein, the original synthesis of  $\text{ZnFe}_2\text{O}_4/\gamma\text{-Fe}_2\text{O}_3$  nanopowders by laser pyrolysis is proposed, and their electrochemical performance as negative electrode materials for Li-ion batteries is evaluated. The effect of different electrolytes and electrode formulations was also studied in order to better understand the cycling mechanism and the cycle life of this promising material.

### Experimental section

#### - $\text{ZnFe}_2\text{O}_4/\gamma\text{-Fe}_2\text{O}_3$ synthesis by laser pyrolysis

During the laser pyrolysis synthesis, an aerosol of the solution containing the precursors produced by a nebulizer is flown into a reactor with a carrier gas. In the reactor, a  $10.6\ \mu\text{m}$   $\text{CO}_2$  laser beam decomposes the precursors producing nanopowders which are then collected on a filter (fig.1). Further details about this process were given by D'Amato *et al.*<sup>14</sup>.

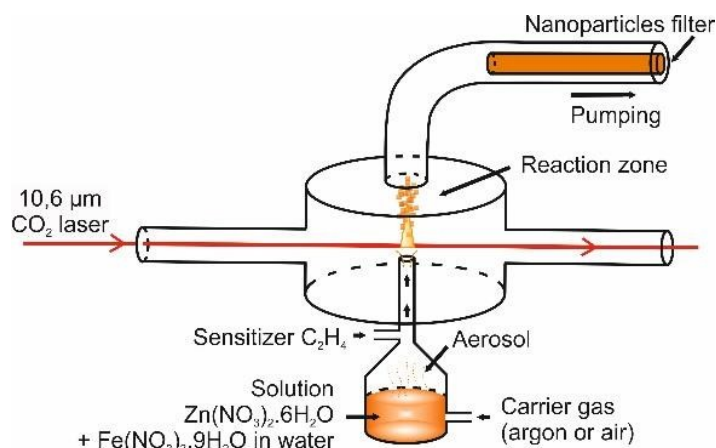


**Figure 1. Laser pyrolysis experimental setup**

A solution of  $\text{Zn}(\text{NO}_3)_2 \cdot 6\text{H}_2\text{O}$  and  $\text{Fe}(\text{NO}_3)_3 \cdot 9\text{H}_2\text{O}$  precursors (1 mol of zinc nitrate for 2 mol of Fe nitrate) dissolved in deionized water was used for the synthesis of  $\text{ZnFe}_2\text{O}_4/\gamma\text{-Fe}_2\text{O}_3$  nanoparticles. The amount of precursors was limited to 50% wt. of the total solution in order to avoid clogging of the spraying nozzle upon long lasting experiments. Ethylene was used as a sensitizer gas to absorb the  $\text{CO}_2$  laser and allow the decomposition of the precursors which do not absorb this laser wavelength. Air was used as the carrier gas, it was chosen for its combustion reaction with  $\text{C}_2\text{H}_4$  that enhances oxidization of Zn and Fe (avoiding suboxide phases formation), increases the reaction temperature (enhancing crystallization), and limits carbon pollution deriving from  $\text{C}_2\text{H}_4$  decomposition. Carrier air flow also serves as spraying gas in the nozzle: as a consequence its flow has to be high enough to generate the aerosol. This latter condition fixed the air flow instead of stoichiometry consideration regarding combustion reaction with  $\text{C}_2\text{H}_4$ . Experimental conditions are summarized in the table 1.

**Table 1. Experimental conditions**

	<b>C<sub>2</sub>H<sub>4</sub> flow rate (sccm)</b>	<b>Air flow rate (sccm)</b>	<b>Laser power source (W)</b>	<b>Feeding rate (g/h)</b>
<b>ZnFe<sub>2</sub>O<sub>4</sub>/Fe<sub>2</sub>O<sub>3</sub></b>	220	5600	1630	10.2

- Materials characterizations

The crystalline phases of the sample were identified by powder X-ray diffraction (XRD, Cu K $\alpha$  = 1.54Å, with a step size of 0.04° over a 2 $\theta$  range of 20°-80°). X-ray photoelectron spectra (XPS) were recorded to establish the valence states of Zn and Fe elements in the sample. <sup>57</sup>Fe Mössbauer spectroscopy was used to determine the nature and the relative amounts of iron containing phases. Transmission <sup>57</sup>Fe Mössbauer spectra were recorded at room temperature with a <sup>57</sup>Co(Rh)  $\gamma$ -ray source in the constant acceleration mode. The velocity scale was calibrated using the magnetic six line spectrum of a high-purity iron absorber. The values of isomer shift ( $\delta$ ), quadrupole splitting ( $\Delta_{EQ}$ ), hyperfine magnetic field ( $B_{HF}$ ) full line width at half-maximum ( $\Gamma$ ) and relative resonance area (RA), determined by fitting the experimental data to appropriate combinations of Lorentzian lines with a nonlinear least-square method. The values of the isomer shift ( $\delta$ ) are given relative to  $\alpha$ -Fe. Scanning electron microscopy (SEM) and transmission electron microscopy (TEM) observations were performed to study the particles morphology and high-resolution transmission electron microscopy (HRTEM) images were used to identify the interplanar distances for the different phases.

- Electrochemical measurements

Electrodes were prepared using ZnFe<sub>2</sub>O<sub>4</sub>/ $\gamma$ -Fe<sub>2</sub>O<sub>3</sub> (with their specific amount deduced from Mössbauer spectrometry) as the active material (70% wt.), CMC (carboxymethyl cellulose) as the binder (12% wt.), and different types of carbon additives to increase conductivity (18% wt.). As summarized in table 2, for some electrodes only carbon black additive is used while in others VGCF (vapor-grown carbon nanofibers) was also added. All these components were suspended with water and mixed in a low-energy ball-mill for 30 minutes (Fritsch Planetary Micro Mill PULVERISETTE 7). Ball-milling was used to obtain more homogeneous electrodes that show better and more reproducible performance compared with other ways of preparation, such as magnetic stirring, due to a better contact between each component of the electrode. TEM images (not shown here) confirm that the morphology of the nanoparticles is still the same after the ball-milling process. The slurry was tape casted on a copper foil with a thickness of 150  $\mu$ m using a doctor blade. After drying the coating overnight at 65°C in an oven, electrodes of 16 mm diameter were cut out of the electrode film and dried again in vacuum for 12h. Half cells vs. lithium metal were assembled in a glovebox using two different electrolytes: EC PC 3DMC + 1M LiPF<sub>6</sub> or EC DMC + 1M LiPF<sub>6</sub>. The electrode loading is around 1.2 mg/cm<sup>2</sup> of active material.

**Table 2. Electrodes composition**

	<b>Electrode CB</b>	<b>Electrode CB-VGCF</b>
<b>Active material</b>	ZnFe <sub>2</sub> O <sub>4</sub> /γ-Fe <sub>2</sub> O <sub>3</sub> – 70%	ZnFe <sub>2</sub> O <sub>4</sub> /γ-Fe <sub>2</sub> O <sub>3</sub> – 70%
<b>Binder</b>	CMC – 12%	CMC – 12%
<b>Additives</b>	Carbon black (Super P) – 18%	Carbon black (Super P) – 9%
		VGCF – 9%

Galvanostatic cycling tests at different current rates (from 20 to 1000 mA/g, respectively around C/50 and 1C) and C-rate from 0.01V to 3.0V were performed with the different electrodes and electrolytes to compare their influence on the battery performance (MTI Neware). Cyclic voltammetry curves were studied to understand the storage mechanism and were performed with a scan rate of 0.1 mV/s between 0.01 and 3.0V (Solartron).

## Results and discussion

### - Powder characterization

The XRD pattern of the obtained sample reveals the presence of two distinct crystalline phases corresponding to ZnFe<sub>2</sub>O<sub>4</sub> Franklinite (JCPDS Card #22-1012) and γ-Fe<sub>2</sub>O<sub>3</sub> maghemite (JCPDS Card #39-1346) (fig.2). The diffraction peaks are quite broadened (0.5-0.6°) suggesting small and/or low crystallinity particles. XPS survey analyses show the peaks of Zn, Fe, O and C (pollution), which are coherent with the phases determined by XRD (fig.3a). The Zn<sup>2p<sub>3/2</sub></sup> and Zn<sup>2p<sub>1/2</sub></sup> spectra are characteristic of Zn<sup>2+</sup> valence state with the peaks at 1022.41 eV and 1045.40 eV, respectively<sup>15</sup> (fig.3b). The Fe spectrum is composed of two peaks at 711.87 eV (Fe<sup>2p<sub>3/2</sub></sup>) and 725.53 eV (Fe<sup>2p<sub>1/2</sub></sup>) which can be attributed to Fe<sup>3+</sup>, and the satellite at 719.69 eV is typical of Fe<sub>2</sub>O<sub>3</sub> (fig.3c)<sup>16</sup>. <sup>57</sup>Fe Mössbauer spectroscopy confirms the presence of two contributions (fig.3d): the main one, accounting for 65% of the total resonance area, is a quadrupole doublet, while the remainder of the spectrum (35%) undergoes magnetic splitting into a distribution of Zeeman sextets. The doublet has typical parameters of superparamagnetic nanosized ZnFe<sub>2</sub>O<sub>4</sub> particles<sup>17-19</sup>, while the magnetically ordered portion can be fitted with at least three magnetic sextets having virtually the same isomer shift and different hyperfine fields (42, 48 and 50 T). These sextets can be assigned to γ-Fe<sub>2</sub>O<sub>3</sub><sup>20</sup> particles with different particle sizes. Fitted parameters are shown in table 3. In particular, Mössbauer spectroscopy shows that the 65% of the iron is contained in ZnFe<sub>2</sub>O<sub>4</sub>, the remainder 35% forming Fe<sub>2</sub>O<sub>3</sub>. Taking into account the theoretical capacities of the two phases (1001 and 1007 mAh.g<sup>-1</sup> for ZnFe<sub>2</sub>O<sub>4</sub> and Fe<sub>2</sub>O<sub>3</sub>, respectively), one can thus calculate the theoretical capacity for the studied sample (1002 mAh.g<sup>-1</sup>). The morphology of the sample is derived from SEM (fig.4a) and TEM images (fig.4b-c), both showing agglomerated small particles (few tens to a hundred of nanometers) together with large particles (more than 500 nm). HRTEM confirms the composition of the powder, with particles showing either the interplanar distance characteristic of γ-Fe<sub>2</sub>O<sub>3</sub> (d=0.210 nm, (400) plane) or the two interplanar distances corresponding to ZnFe<sub>2</sub>O<sub>4</sub> (d= 0.263 nm for (310) plane, d= 0.220 nm for (321) plane) (fig.4d-e). Besides, HRTEM identifies the two phases in both small and large particles, highlighting that there is no preferential composition corresponding to one population size. In summary, these results clearly indicate that the obtained powder is composed of a homogeneous and intimate mixture of separate particles of the two phases.

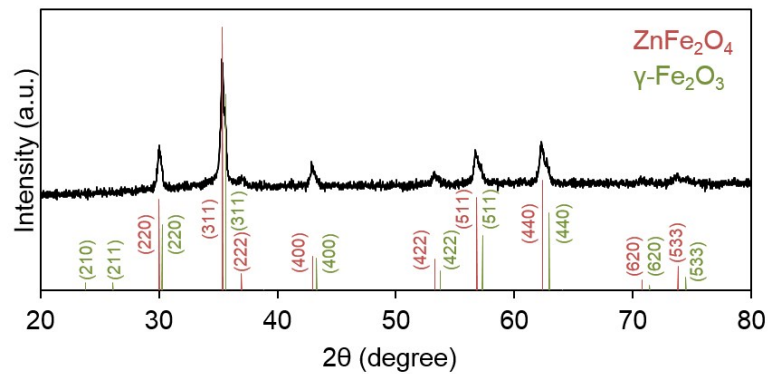


Figure 2. XRD pattern for  $\text{ZnFe}_2\text{O}_4/\gamma\text{-Fe}_2\text{O}_3$  obtained by laser pyrolysis

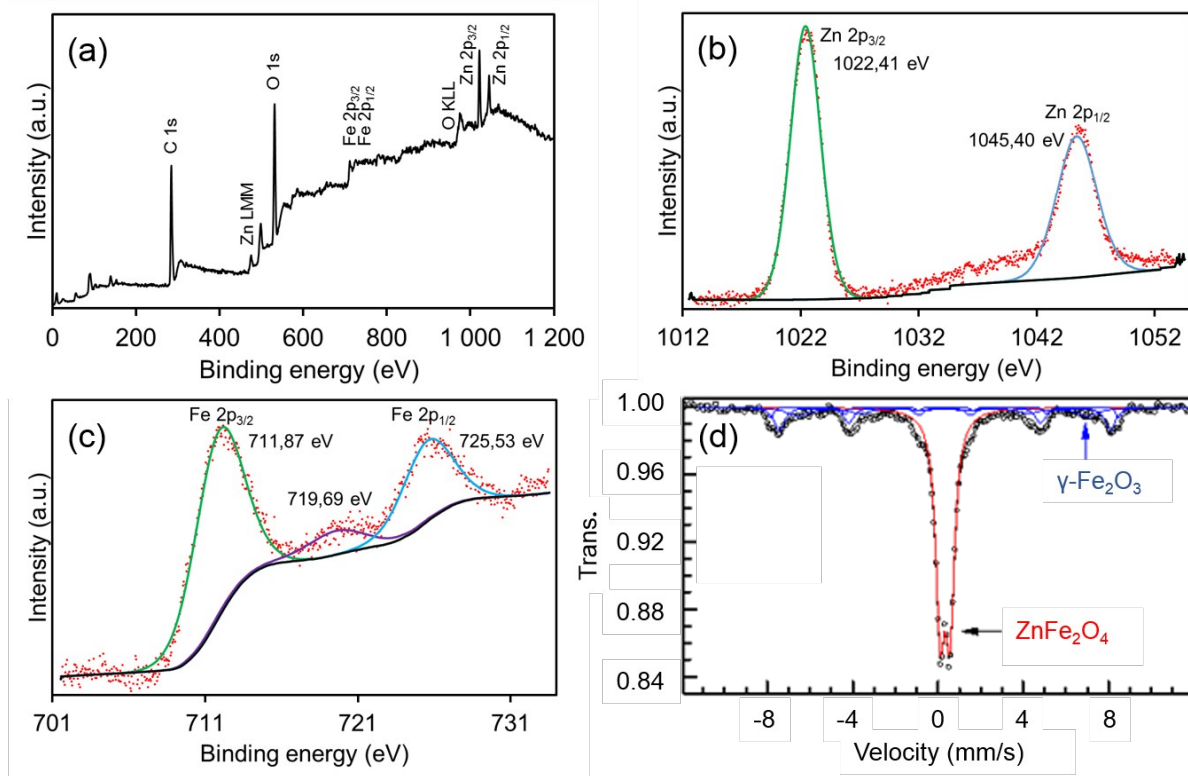
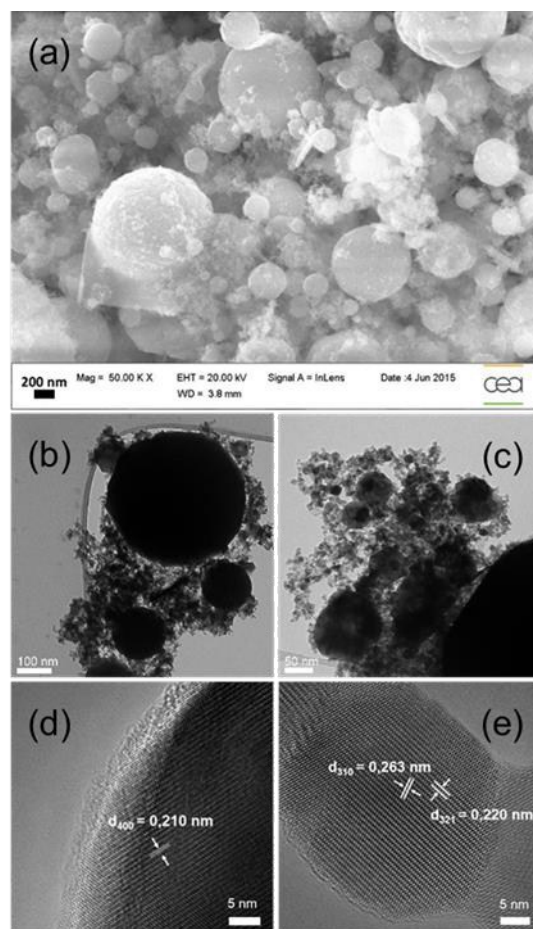


Figure 3. XPS spectra for  $\text{ZnFe}_2\text{O}_4/\gamma\text{-Fe}_2\text{O}_3$  obtained by laser pyrolysis (a: survey, b: Zn spectrum, c: Fe spectrum) and room temperature  $^{57}\text{Fe}$  Mössbauer spectrum showing the presence of both  $\text{ZnFe}_2\text{O}_4$  (65% at.) and  $\gamma\text{-Fe}_2\text{O}_3$  (35% at.) phases (d)

Table 3.  $^{57}\text{Fe}$  Room temperature Mössbauer parameters. (\*) indicates average values.

	$\delta$ (mm/s)	$\Delta_{\text{EQ}}$ (mm/s)	$\Gamma$ (mm/s)	$B_{\text{HF}}$ (Tesla)	RA (%)
Doublet	0.34	0.46	0.50	-	65
Sextets	0.30*	-0.03	0.82*	42,48 and 50.6	35



**Figure 4. Particles morphology observed by SEM (a) and TEM (b, c) revealing two size populations and presence of the different phases revealed by HRTEM (d,e)**

The presence of both  $\text{ZnFe}_2\text{O}_4$  and  $\text{Fe}_2\text{O}_3$  was not expected as the solution containing the precursors was prepared in a stoichiometric ratio. However, the pyrolytic decomposition process of ferrite powders is known to lead to many intermediate products such as  $\text{ZnO}$ ,  $\text{Fe}_2\text{O}_3$  and stoichiometric  $\text{ZnFe}_2\text{O}_4$ <sup>18,21</sup>. Moreover, what can be highlighted in these results is the specific morphology with the two size populations which is not commonly observed for laser pyrolysis grown nanoparticles. This appears to be a specific trend when using Fe nitrate precursor while chloride or acetylacetonate precursors lead to only one size population with small nanoparticles<sup>22</sup>. The two populations could possibly result from two different but simultaneous growth processes. When the aerosol droplets enter the reaction zone, the solvent is vaporized and the dissolved salts form dry spherical objects. Upon heating, a solid phase reaction can take place within these particles leading to large nanostructured spherical particles. In the specific case of laser pyrolysis, the heating rate is very fast upon interacting with the laser beam and the energy density encountered by the dried particles is very high, especially with a focused beam. In that case, part of the solid salt could be vaporized before reacting, leading to a gas phase reaction (nucleation and growth) which would form small nanoparticles agglomerated in chain-like poorly dense structures<sup>14</sup>. This latter vaporization phenomenon could take place at the surface of the dried particles simultaneously to the solid state reaction occurring in the core of the particles (fig.5).

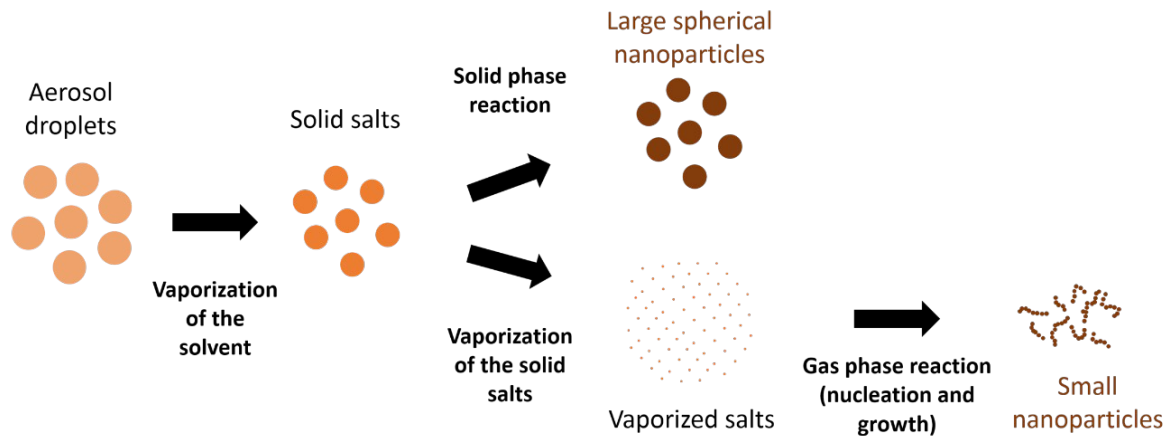


**Figure 5. Possible growth processes during laser pyrolysis conducting to a bimodal particle size distribution**

- Electrochemical performance

The active material consists of  $\text{ZnFe}_2\text{O}_4$  (65% at.) and  $\text{Fe}_2\text{O}_3$  (35% at.), providing a global theoretical specific capacity of 1002 mAh/g. This value is calculated by taking into account the specific capacity of both phases (1000 mAh/g for  $\text{ZnFe}_2\text{O}_4$  and 1007 mAh/g for  $\text{Fe}_2\text{O}_3$ <sup>23</sup>) and their weight ratio. The electrochemical performance of  $\text{ZnFe}_2\text{O}_4/\text{Fe}_2\text{O}_3$  was evaluated in the galvanostatic mode with an electrode containing both CB and VGCF as conducting additives and with EC-PC-3DMC + 1M  $\text{LiPF}_6$  electrolyte, at C/10 current rate between 0.01V and 3.0 V (fig.6a). A coulombic efficiency of 66% was obtained after the first cycle, which is low but rather common for transition metal oxides electrodes<sup>7,24,25</sup>. The first lithiation capacity of 1706 mAh/g is higher than the theoretical capacity and the additional capacity could be explained by some parasitic reactions of the electrolyte at low potential that create a solid electrolyte interphase (SEI) as well as a polymeric gel-type layer around the nanoparticles, which irreversibly trap a part of the lithium<sup>26</sup>. These two phenomena lead to an irreversible capacity of 576 mAh/g at the first cycle, with a charge capacity of 1130 mAh/g that is still higher than the theoretical capacity. A slow decrease of the reversible capacity is then observed for the 16 following cycles, probably due to additional lithium trapping into the unstable solid electrolyte interface. Nevertheless, after about 20 cycles, the reversible capacity progressively increases to about 1210 mAh/g after 100 cycles which is still 200 mAh/g higher than the theoretical capacity. Such behavior is not uncommon for transition metal oxides and has been reported for  $\text{Fe}_2\text{O}_3$ <sup>27</sup>,  $\text{Fe}_3\text{O}_4$ <sup>28</sup> and  $\text{ZnFe}_2\text{O}_4$ <sup>10</sup>. This effect has been attributed in the literature to the reversible reaction of a polymeric gel-type layer formed by the partial decomposition of the electrolyte, kinetically activated by the electrode material at the electrode/electrolyte interface. The existence of such an active layer accounts for the additional capacity of the electrodes, largely exceeding the theoretical one<sup>8,29,30,31,32</sup>. The coulombic efficiency during this cycling is relatively stable despite the increase of the capacity, with an average efficiency of 98.9% for the last fifty cycles. The voltage vs. capacity curves (fig.6b) also reveal this increase of capacity, showing a reversible capacity for the 100<sup>th</sup> cycle higher than for the 10<sup>th</sup> one. At the first lithiation, a slope can be observed from 3.0 to 0.8 V, followed by a long plateau at 0.8 V, corresponding to a lithiation capacity of 150 mAh/g (~1.4 mol Li) and 950 mAh/g (~8.6 mol Li), respectively. Based on previous results<sup>13</sup>, the first 150 mAh/g of capacity may correspond to the lithium insertion in the oxide structure whereas the conversion reaction takes place at 0.8 V. Between 0.8 to 0.01 V, a capacity of 600 mAh/g (~5.4 mol Li) is obtained which can be explained by the formation of the solid electrolyte interphase and the polymeric gel-type layer around

the metallic particles along with reactions with the electrolyte. The plateau at 0.8 V becomes shorter in the next cycles and the main part of the capacity is due to reactions occurring below after 0.8 V. The electrochemical signature below 0.8 increases with time, partly explaining the observed increase in capacity.

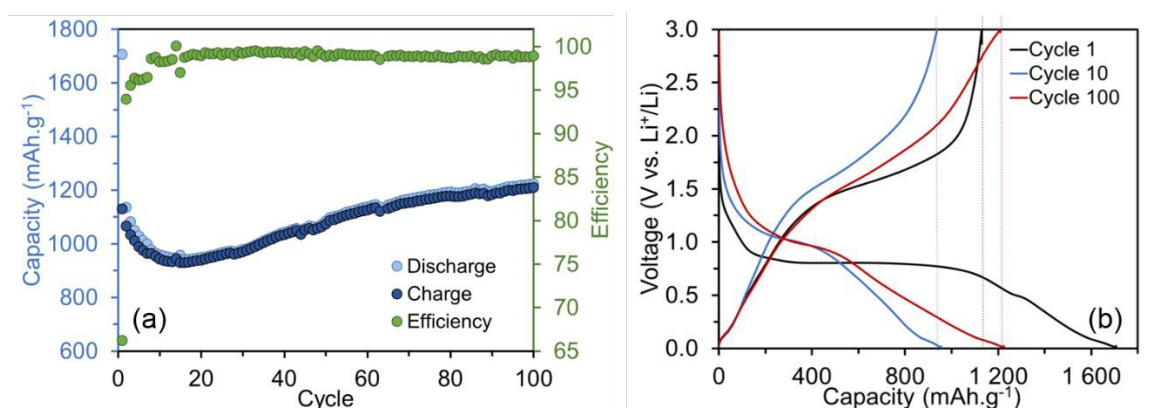


**Figure 6. Galvanostatic cycles at C/10 (a), voltage vs capacity curves between 0.01V and 3.0V at C/10 (b)**

To test the cyclability of the material at a higher current rate, electrodes similar to the previous one were cycled at C/90 current rate for the first cycle (which helps to form a more stable SEI at the beginning and have a fully lithiated material) and then 200 cycles at C/2 (500 mA/g) current rate have been performed (fig.7). A first discharge capacity of 1520 mAh/g was obtained at C/90 current rate which is quite close to the capacity measured at C/10. At C/2, the reversible capacity decreases steadily during the first hundred cycles before stabilizing around 360 mAh/g in the following 200 cycles. The average coulombic efficiency in the last 200 cycles is stable at 99.25%. Although the capacity is drastically reduced at C/2, the ZnFe<sub>2</sub>O<sub>4</sub>/Fe<sub>2</sub>O<sub>3</sub> electrode is able to give a very stable capacity for hundreds cycles with a good efficiency.

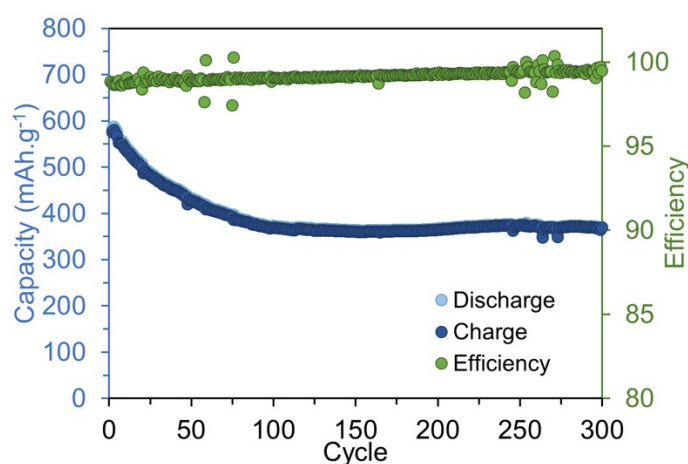


**Figure 7. Capacity retention at C/2 (after one cycle at C/90)**

A study of the rate capability was also performed to demonstrate the stability of the material. The current density was increased in several steps after every five cycles from C/45 (20 mA/g) to 4C (4000 mA/g) for the fastest cycles and then decreased directly to C/45 (fig.8). The specific capacity decreases with increasing current rate. The electrode shows a very good cyclability with a reversible capacity varying from 876 to 422 mAh/g. At the second C/45 current density, the material recovers a higher specific capacity than for the first cycles.

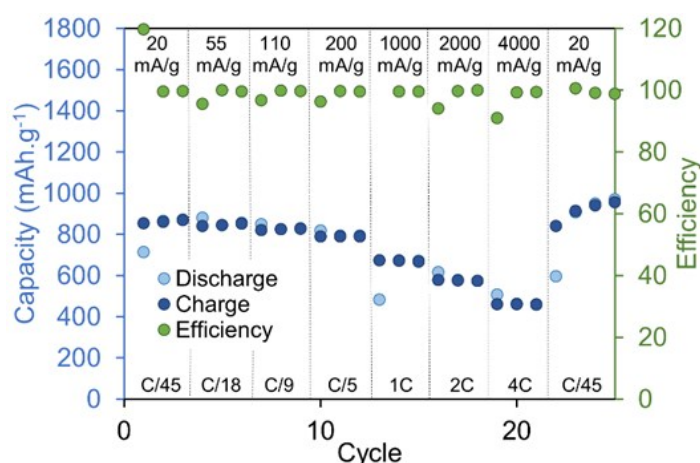


**Figure 8. C-rate C/45, C/18, C/9, C/5, 1C, 2C and 4C current rates**

To better identify the potential of each electrochemical process during the lithiation and delithiation processes, cyclic voltammograms were realized using an electrode containing both CB and VGCF and EC PC 3DMC + 1M LiPF<sub>6</sub> electrolyte (fig.9). The first lithiation curve shows a reduction peak around 0.55 V which can probably be attributed to the insertion of lithium inside the crystalline structure leading to its amorphization and to the conversion reaction with Zn(II) and Fe(III) which are reduced to Zn(0) and Fe(0). The first delithiation curve then shows an anodic peak at 1.6 V which may correspond to the oxidization of Zn(0) and Fe(0) to Zn(II) and Fe(III)<sup>33,34,35,36</sup>. After the first cycle, the cathodic peak shifts from 0.55 to 0.94 V. This is in agreement with the discharge potential plateau located approximately at 1.0 V after the first cycle in fig.5b. This potential shift is characteristic of conversion-type reactions and is related to the replacement of the conversion potential plateau in first discharge by a mostly sloping curve corresponding to the cycling of the *in situ* formed nanomaterial. Another contribution to the drastic changes in voltage between discharge and charge in the first cycle has an origin in the amorphous character for the Li<sub>2</sub>O/M (M=Fe, Zn) nanocomposite (see the proposed mechanism below) at the end of discharge which implies differences in free energy, and, therefore, in equilibrium reaction potential.

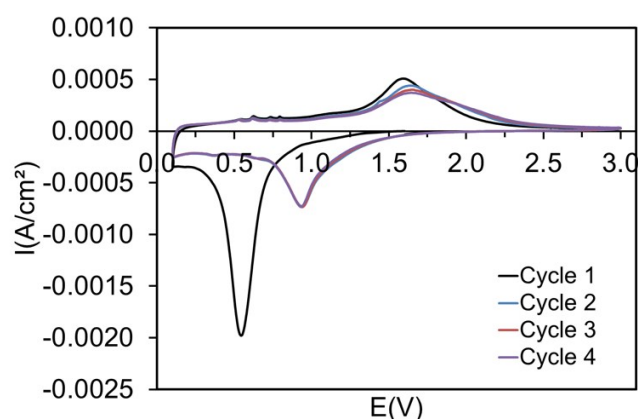
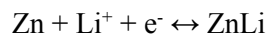


**Figure 9. CV measurements at 0.1mV/s scan rate between 0.01V and 3.0V**

Concerning the lithium storage mechanism in ZnFe<sub>2</sub>O<sub>4</sub>, assumptions were made by different authors<sup>5,9</sup>: insertion of lithium in the material should occur first, leading to a Li<sub>x</sub>ZnFe<sub>2</sub>O<sub>4</sub> phase with  $x \leq 2$ ; on advancing lithiation, the material undergoes the conversion reaction, with a complete loss of the crystalline structure, and the expected formation of Zn and Fe nanoparticles embedded in a Li<sub>2</sub>O matrix. In the final part of the discharge, Zn is

expected to alloy with Li to form ZnLi. It is also supposed that, after the first cycle, ZnFe<sub>2</sub>O<sub>4</sub> is not recovered but instead nanometric forms of ZnO and Fe<sub>2</sub>O<sub>3</sub> are formed as the final delithiated phases. Subsequent cycling is then between these phases and the species obtained at the end of the first discharge, which explains the difference in electrochemical signature between the first and the following lithiations:



These reactions, however, do not explain the reversible capacity exceeding the theoretical one and gradually increasing for our material. Several assumptions can be made to explain this phenomenon: the specific nanosized morphology obtained by laser pyrolysis, for instance, may allow specific surface related storage even after the first conversion reaction, which produces a massive morphological re-configuration of the cycling material<sup>10</sup>; the presence of carbon additives in the electrode can also contribute to the capacity (taking into account that there is 18% of carbon additives in the electrode, an additional reversible contribution up to 60 mAh/g can be considered<sup>37</sup>). Besides, with the electrolyte degradation during cycling, the reversible formation of a polymeric gel-type layer around the nanoparticles can also explain the excess capacity delivered at low potential<sup>38</sup>, another assumption is that the solid electrolyte interphase can work as an extra-charge reservoir for lithium<sup>39</sup>. To understand if either the nature of the electrolyte or of the carbon additives have an impact on the increasing capacity, galvanostatic cycles at C/10 were realized with and without VGCF and using a different electrolyte: EC DMC + 1M LiPF<sub>6</sub> (fig.10a). The results reveal that the change of solvent mixture in the electrolyte has no effect on the increase of reversible capacity in cycling but it seems that EC PC 3DMC + 1M LiPF<sub>6</sub> produces a higher specific capacity than EC DMC + 1M LiPF<sub>6</sub>. Concerning the influence of VGCF at C/10, no increase of capacity is observed without VGCF during the first hundred cycles. However, at 1C current rate (fig.10b), the cycling was made with a CB electrode and a slight but significant increase of capacity can be observed even without VGCF. Reversible reactions with the electrolyte may occurred during the cycling, leading to this increase phenomenon, sometimes enhanced by the VGCF addition and favored by the specific particles morphology obtained by laser pyrolysis.

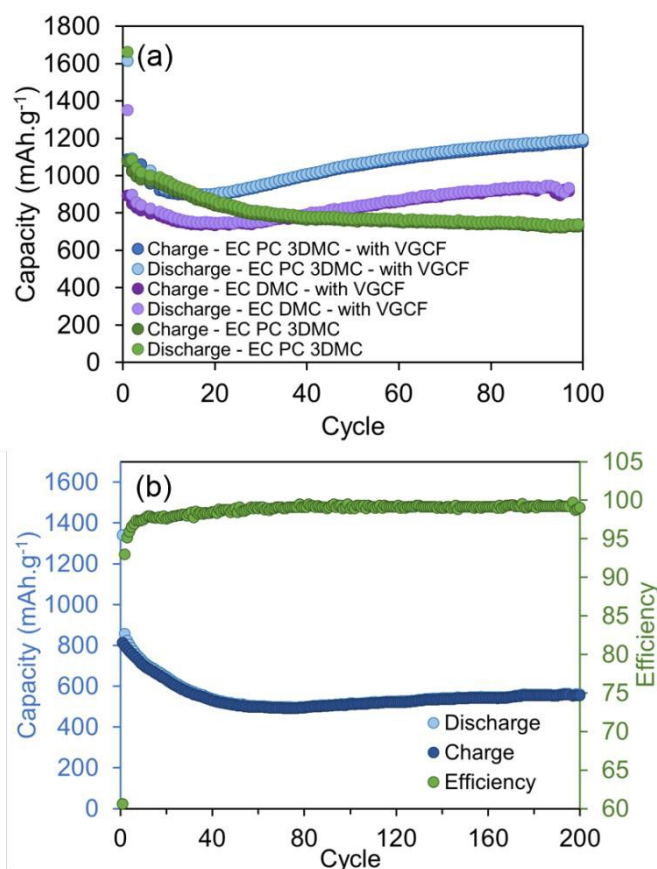


**Figure 10. Influence of VGCF and electrolytes on the cycling performance (a) and galvanostatic cycling at 1C current rate without VGCF (b)**

## Conclusion

To summarize, ZnFe<sub>2</sub>O<sub>4</sub>/Fe<sub>2</sub>O<sub>3</sub> nanopowder was synthesized by laser pyrolysis. The obtained powder shows a particular morphology constituted by agglomerated particles with a bimodal size distribution, which is attributed to the use of iron nitrate precursor. Compared with performances of pure ZnFe<sub>2</sub>O<sub>4</sub>, this ZnFe<sub>2</sub>O<sub>4</sub>/Fe<sub>2</sub>O<sub>3</sub> nanocomposite shows a good performance as negative electrode material in half cells vs. lithium metal: at C/10 rate, the material exhibits a first lithiation capacity above 1700 mAh/g and more than 1100 mAh/g still remains after the first delithiation. Surprisingly the reversible capacity increases with the number of cycles at C/10 current rate leading to more than 1200 mAh/g after 100 cycles, which is significantly higher than the theoretical capacity. This overcapacity can be explained by an additional reversible redox reaction caused by electrolyte degradation, which is perhaps favored by the particular morphology of the particles and by the VGCF additive in the electrode formulation. This phenomenon is not observed at higher current rates. The influence of the electrolyte and of the addition of VGCF on the battery performance was also studied. The use of EC PC 3DMC + 1M LiPF<sub>6</sub> electrolyte allows the material to keep a higher specific capacity and does not affect the increase phenomenon. The VGCF helps obtaining a higher reversible capacity after several cycles and seems to have an effect on the overcapacity phenomenon depending on the chosen current rate. In spite of these observations, the ZnFe<sub>2</sub>O<sub>4</sub>/Fe<sub>2</sub>O<sub>3</sub> composite prepared by laser pyrolysis demonstrates a promising performance as a possible next generation of lithium-ion battery negative electrode.

## Acknowledgements

This work was supported by the CEA Advanced Materials Cross Cutting Program. The authors gratefully acknowledge Dr. Servane Coste-Leconte for the access to XRD facilities, the TEM team (CEA-DSV) for TEM access as well as Jocelyne Leroy (CEA/IRAMIS/NIMBE) for XPS characterizations and Rémi Chassagnon (Laboratoire Interdisciplinaire Carnot de Bourgogne, UMR 6303) for HRTEM access.

## References

- 1 J. Cabana, L. Monconduit, D. Larcher and M. R. Palacín, *Adv. Mater.*, 2010, **22**, E170–92.
- 2 M. V Reddy, T. Yu, C. H. Sow, Z. X. Shen, C. T. Lim, G. V Subba Rao and B. V. R. Chowdari, *Adv. Funct. Mater.*, 2007, **17**, 2792–2799.
- 3 M. Chen, X. Xia, J. Yin and Q. Chen, *Electrochim. Acta*, 2015, **160**, 15–21.
- 4 Y. Chen, H. Xia, L. Lu and J. Xue, *J. Mater. Chem.*, 2012, **22**, 5006.
- 5 C. Yuan, H. Bin Wu, Y. Xie and X. W. D. Lou, *Angew. Chem. Int. Ed. Engl.*, 2014, **53**, 1488–1504.
- 6 X. Guo, X. Lu, X. Fang, Y. Mao, Z. Wang, L. Chen, X. Xu, H. Yang and Y. Liu, *Electrochem. commun.*, 2010, **12**, 847–850.
- 7 P. F. Teh, Y. Sharma, S. S. Pramana and M. Srinivasan, *J. Mater. Chem.*, 2011, **21**, 14999.
- 8 H. Xia, Y. Qian, Y. Fu and X. Wang, *Solid State Sci.*, 2013, **17**, 67–71.
- 9 L. Yao, X. Hou, S. Hu, J. Wang, M. Li, C. Su, M. O. Tade, Z. Shao and X. Liu, *J. Power Sources*, 2014, **258**, 305–313.
- 10 X. Hou, X. Wang, L. Yao, S. Hu, Y. Wu and X. Liu, *New J. Chem.*, 2015, **39**, 1943–1952.
- 11 D. Bresser, E. Paillard, R. Kloepsch, S. Krueger, M. Fiedler, R. Schmitz, D. Baither, M. Winter and S. Passerini, *Adv. Energy Mater.*, 2013, **3**, 513–523.
- 12 Z. Xing, Z. Ju, J. Yang, H. Xu and Y. Qian, *Nano Res.*, 2012, **5**, 477–485.
- 13 Y. Sharma, N. Sharma, G. V. S. Rao and B. V. R. Chowdari, *Electrochim. Acta*, 2008, **53**, 2380–2385.
- 14 R. D'Amato, M. Falconieri, S. Gagliardi, E. Popovici, E. Serra, G. Terranova and E. Borsella, *J. Anal. Appl. Pyrolysis*, 2013, **104**, 461–469.
- 15 L. Lian, L. Hou, L. Zhou, L. Wang and C. Yuan, *RSC Adv.*, 2014, **4**, 49212–49218.
- 16 X. Wang, Y. Xiao, C. Hu and M. Cao, *Mater. Res. Bull.*, 2014, **59**, 162–169.
- 17 Y. Ahn, E. J. Choi, S. Kim, D. H. An, K. U. Kang, B. G. Lee, K. S. Baek and H. N. Oak, *J. Korean Phys. Soc.*, 2002, **41**, 123–128.
- 18 J. Kurian, S. P. John, M. M. Jacob, V. R. Reddy, K. E. Abraham and V. S. Prasad, *IOP Conf. Ser. Mater. Sci. Eng.*, 2015, **73**, 12032.
- 19 G. F. Goya and H. R. Rechenberg, *J. Magn. Magn. Mater.*, 1999, **196–197**, 191–192.
- 20 P. M. A. de Bakker, E. De Grave, R. E. Vandenberg, L. H. Bowen, R. J. Pollard and P. R.M., *Phys. Chem.*

- Miner.*, 1991, **18**, 131–143.
- 21 Y. Li, J. Zhao, J. Jiang and J. Han, *Mater. Res. Bull.*, 2003, **38**, 1393–1399.
- 22 T. González-Carreño, M. P. Morales, M. Gracia and C. J. Serna, *Mater. Lett.*, 1993, **18**, 151–155.
- 23 S.-H. Yu, S. H. Lee, D. J. Lee, Y.-E. Sung and T. Hyeon, *Small*, 2015, n/a--n/a.
- 24 X. Yao, J. Kong, X. Tang, D. Zhou, C. Zhao, R. Zhou and X. Lu, *RSC Adv.*, 2014, **4**, 27488.
- 25 S. H. Choi and Y. C. Kang, 2013, **8**, 6281–6290.
- 26 E. Peled, *J. Electrochem. Soc.*, 1979, **126**, 2047–2051.
- 27 E. Environ, 2012, 5252–5256.
- 28 J. Xu and Y. Zhu, 2012, 2–7.
- 29 G. Zhou, D. W. Wang, F. Li, L. Zhang, N. Li, Z. S. Wu, L. Wen, G. Q. Lu and H. M. Cheng, *Chem. Mater.*, 2010, **22**, 5306–5313.
- 30 S. Laruelle, S. Grugeon, P. Poizot, M. Dollé, L. Dupont and J. Tarascon, 2017, **160**, 149–150.
- 31 J. S. Do and C. H. Weng, *J. Power Sources*, 2005, **146**, 482–486.
- 32 S. J. Rezvani, R. Gunnella, A. Witkowska, F. Mueller, M. Pasqualini, F. Nobili, S. Passerini and A. Di Cicco, *ACS Appl. Mater. Interfaces*, 2017, **9**, 4570–4576.
- 33 Y. Ding, Y. Yang and H. Shao, *Electrochim. Acta*, 2011, **56**, 9433–9438.
- 34 N. Wang, H. Xu, L. Chen, X. Gu, J. Yang and Y. Qian, *J. Power Sources*, 2014, **247**, 163–169.
- 35 Y. Zhang, C. J. Pelliccione, A. B. Brady, H. Guo, P. F. Smith, P. Liu, A. C. Marschilok, K. J. Takeuchi and E. S. Takeuchi, *Chem. Mater.*, 2017, **29**, 4282–4292.
- 36 D. Zhou, H. Jia, J. Rana, T. Placke, T. Scherb, R. Kloepsch, G. Schumacher, M. Winter and J. Banhart, *Electrochim. Acta*, 2017, **246**, 699–706.
- 37 PhD. Marino, Cyril. Optimisation de nouvelles électrodes négatives énergétiques pour batteries lithium-ion : caractérisation des interfaces électrode/électrolyte. Montpellier : 2012. Université de Montpellier 2.
- 38 S. Grugeon, S. Laruelle, L. Dupont and J. Tarascon, 2003, **5**, 895–904.
- 39 S. J. Rezvani, R. Gunnella, A. Witkowska, F. Mueller, M. Pasqualini, F. Nobili, S. Passerini and A. Di Cicco, 2017.